

Modeling curved fibers by fitting R-vine copulas to their Frenet representations

Matthias Weber,¹ Andreas Grießer,² Erik Glatt,² Andreas Wiegmann,² and Volker Schmidt¹

¹*Institute of Stochastics, Ulm University, Helmholtzstraße 18, 89069 Ulm, Germany*

²*Math2Market GmbH, Richard-Wagner-Straße 1, D-67655, Kaiserslautern, Germany*

Corresponding Author: Matthias Weber <matthias.weber@uni-ulm.de>

Abstract

In the present paper, we propose a novel single-fiber model which exploits a description of fibers as a sequence of bond and torsion angles. Using the Frenet-Serret formulas, this representation can be translated into 3D space and vice-versa. While the precise locations of points along a fiber do not directly convey information about inner material properties of the fiber, the distribution of bond and torsion angles may be related to various material characteristics and, thus, our model may form a direct link between inner material properties and emerging microstructure properties. More precisely, we model curved fibers in the three-dimensional Euclidean space \mathbb{R}^3 as polygonal tracks that we represent by their local curvature and torsion at each sampling point. The two-dimensional sequences of curvatures and torsions obtained in this way are then considered as realizations of a Markov chain with finite memory which takes its values in \mathbb{R}^2 . The transition kernel of this Markov chain is given by a family of conditional multivariate probability distributions. They are constructed using so-called R-vine copulas, which are fitted and validated by means of experimental data.

Key Words: stochastic fiber model, Frenet-Serret formula, curvature, torsion, Markov chain, R-vine copula, conditional sampling

1 Introduction

Fiber-based materials play an important role in various application areas, like fuel cell technology (Schulz et al., 2007), filtration (Geerling et al., 2020), light weight materials (Ali et al., 2020), or hygiene products (Kroutilova et al., 2020). For many of these applications, so-called nonwovens are used. The improvement of nonwoven is an expensive and time-consuming technological process. To reduce cost and time for this process, computer models can be exploited to perform the design of the materials digitally. Digital materials design makes use of modern 3D imaging techniques like micro-CT which have enabled the detailed analysis of the microstructure and morphology of fibrous materials. In particular, tomographic imaging techniques are capable of visualizing the fibers constituting the nonwoven materials. For further analysis of the imaged structures, labeling approaches exist to identify individual fibers in the tomographic image data. Recently, convolutional neural networks have successfully been applied to this task (Grießer et al., 2019; Grießer et al., 2022b).

While many properties of fibrous materials can be determined on scanned image data, mathematical modeling of the underlying structure is beneficial for getting a better understanding of microstructure-property relationships (Huang et al., 2017; Schneider, 2017; Venkateshan et al., 2016) and, in this way, for developing new materials with enhanced properties. For the materials considered in the present paper, stochastic modeling has proven capable of grasping the essential structural properties while still being computationally feasible. In particular, by means of stochastic models, a wide spectrum of virtual but realistic fibers can be generated which can be used for the determination of fibrous materials with optimized physical properties and, thus, for the efficient improvement of nonwoven materials. Note that various stochastic models exist for the 3D microstructure and morphology of nonwoven used, e.g., for general purposes (Kallel & Joulain, 2022; Mao et al., 2007; Moghadam et al., 2019; Wiegmann, 2008), in filter media (Abishek et al., 2017; Azimian et al., 2018; Soltani et al., 2017; Wiegmann et al., 2007), as so-called gas diffusion layers in fuel cells (Gaiselmann et al., 2013; Schulz et al., 2007;

Zamel et al., 2010), and for acoustic trim (Schladitz et al., 2006; Soltani et al., 2018). Most of these models are built in two steps, i.e., they consist of a single-fiber model and a framework for combining multiple fibers into the desired structure, where the single-fiber models usually consider the fibers as sequences of points in 3D space and directly describe the relationships between the locations of neighboring points (Altendorf & Jeulin, 2011; Gaiselmann et al., 2013; Townsend et al., 2021).

In the present paper, we propose a novel single-fiber model which exploits a description of fibers as a sequence of bond and torsion angles. Using the Frenet-Serret formulas (Kühnel, 2015), this representation can be translated into 3D space and vice-versa. While the precise locations of points along a fiber do not directly convey information about inner material properties of the fiber, the distribution of bond and torsion angles may be related to various material characteristics and, thus, the model may form a direct link between inner material properties and emerging microstructure properties. To capture correlations along the fibers extracted from tomographic image data, the single-fiber model proposed in this paper consists of a k -th order Markov chain (Raftery, 1985) describing the sequence of bond and torsion angles, where an R-vine copula (Czado, 2019; Joe, 2014) is used to model the transition kernel of the Markov chain. For this, we extract representations of fibers as sequences of bond and torsion angles from measured image data of a nonwoven material, where individual fibers have been identified using the method described in Grießer et al. (2022b). Then, we fit the Markov model mentioned above to the data and validate it by simulating a set of fibers and comparing their structural properties to those observed in experimental data.

The rest of this paper is organized as follows. In Section 2, the underlying measured image data and their preprocessing is described, together with the Frenet representation of fibers extracted from image data and the Markov model for their stochastic modeling. Then, in Section 3, the results obtained in this way are presented. Finally, a discussion of the results and an outlook to possible future research topics is provided in Section 4.

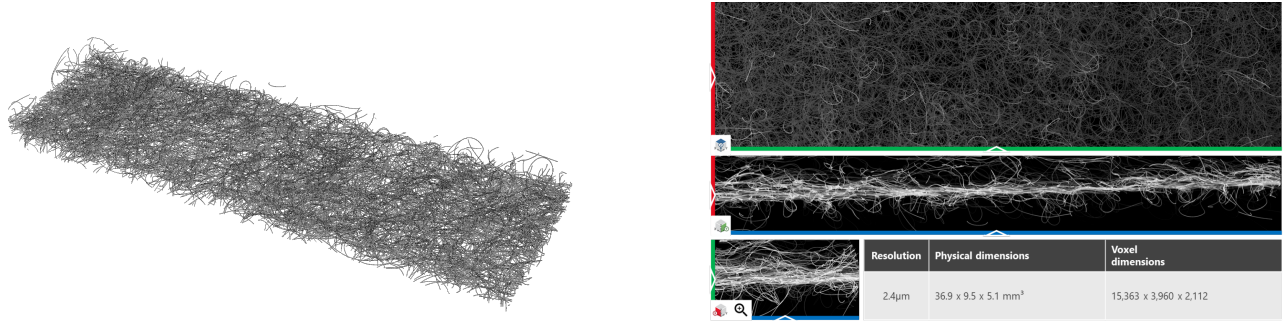


Fig. 1. 3D (left) and 2D (right) views of the sample considered in the present paper – this sample is provided online as scan and identified fibers under Grießer et al. (2022a).

2 Materials and Methods

2.1 Tomographic Image Data and Their Preprocessing

The material under consideration is a bulky nonwoven fabric. According to Kroutilova et al. (2020), the material can be used, for example, in the hygiene industry as various parts of absorbent hygiene products (e.g. baby diapers, incontinence products, female hygiene products, changing pads, etc.) or in healthcare, for instance, as a part of protective garments, surgical cover sheets, underlays and other barrier material products. Further use cases are possible in technical applications, e.g., as a part of protective garments, in filtration, insulation, packaging, sound adsorption, shoe industry, automotive, furniture, etc.

The sample considered in the present paper is composed of synthetic round fibers, see Fig. 1. The fiber diameter varies slightly within the sample around a mean value of 24 μ m. To study this material in detail, multiple scans were acquired by Bruker micro-CT on a SkyScan 1272 with a resolution of 2.4 μ m. These individual scans were stitched together along the x -axis to create the full-sized scan. The complete sample has dimensions of 36.87 mm \times 8.74 mm \times 5.07 mm, or 15 363 px \times 3640 px \times 2112 px for a total of 118 105 827 840 voxels. The sample is available for general access, see Grießer et al. (2022a). The data set contains the original micro-CT scan, the segmented binary raw image, the labeled raw image where every fiber has its own label, and the analytic description of the center lines of the

fibers. In Grießer et al. (2019), a neural network was trained on generated training data and then used to label the center lines of each fiber in the segmented micro-CT scan in order to obtain the individual fibers. In total, 2377 fibers with a maximum length of 12.65 cm and an overall length of 17.09 m were extracted from the data. As short fibers may be susceptible to effects from sample preparation and effects from measuring artefacts, we exclude all fibers shorter than 3 mm from the analysis. This leaves us with 1117 fibers with an overall length of 16.01 m, thus preserving more than 93% of the totaled length.

The extracted fibers are represented by polygonal tracks where nodes are placed such that the overall deviation from the original fiber in the micro-CT scan and the number of nodes is balanced. For the modeling approach chosen in the present paper, equidistant sampling of the fibers, i.e, a constant distance between each pair of neighboring nodes on the polygonal track, is required. We ensure this by creating modified versions of each polygonal track. Given the original polygonal track $x: [0, 1] \rightarrow \mathbb{R}^3$ with nodes $r_i = x(s_i)$ and straight segments in between (i.e. $x(s) = \frac{1}{s_{k+1}-s_k} ((s - s_k)x(s_{k+1}) + (s_{k+1} - s)x(s_k))$ for $s_k < s < s_{k+1}$), the nodes r'_i of the modified track with some sampling length $l > 0$ are given by

$$\begin{aligned} r'_1 &= r_1 \\ r'_{i+1} &= x(\min\{s > s'_i : |x(s) - r'_i| = l\}) \end{aligned}$$

where $x(s'_i) = r'_i$ and $|z|$ denotes the Euclidean norm of $z \in \mathbb{R}^3$. Note that we resample each fiber at a resolution of $l = 0.1$ mm. In the following, to keep the notation possibly simple, the nodes of the modified polygonal tracks will be denoted by r_i (instead of r'_i).

2.2 Frenet Representation

As mentioned above, for purposes of modeling and analysis, curved fibers are often represented as polygonal tracks, i.e., sequences of points in the three-dimensional Euclidean space \mathbb{R}^3 . This generic representation proves useful for measuring and visualizing fibers by, e.g., tomographic

imaging and voxel images, respectively. Extensions of pure polygonal tracks include splines which are often used in computer graphics and modeling (Bartels et al., 1995). They provide means to reduce the number of sampling points and for smooth interpolation of (discrete) curves by introducing a piecewise polynomial representation. These representations, based on a sequence of (sampling) points, provide a global view of fibers but cannot directly model local properties. For providing a direct link between material properties and 3D morphology of the modeled fibers, a representation of discrete curves by local geometrical properties is useful, which is explained in the following.

2.2.1 Continuously Parameterized Curves

Assume that a curve is given by a differentiable function $x : [0, 1] \rightarrow \mathbb{R}^3$. Then, for any $s \in [0, 1]$, the Frenet-Serret formulas (Kühnel, 2015) can be used to compute the curvature $\kappa(s)$ and torsion $\tau(s)$ at each point $x(s) \in \mathbb{R}^3$ along the curve $x = \{x(s), s \in [0, 1]\}$. More precisely, the curvature $\kappa(s)$ and torsion $\tau(s)$ at each point $x(s)$ along the curve are defined via the unit tangent vector $T(s)$, the normal unit vector $N(s)$, and the binormal unit vector $B(s) = T(s) \times N(s)$ at $x(s)$, where $T(s) \times N(s)$ denotes the cross product of the unit vectors $T(s)$ and $N(s)$, and

$$\frac{dT}{ds} = \kappa N, \tag{1}$$

$$\frac{dN}{ds} = -\kappa T + \tau B, \tag{2}$$

$$\frac{dB}{ds} = -\tau N. \tag{3}$$

The orthonormal vectors T, N, B occurring in this system of differential equations are called the *Frenet-Serret frame*. Thus, intuitively speaking, the curvature κ describes the change in direction and the torsion τ describes the local deviation of the curve from a planar curve, i.e., the change in the osculating plane. Note that for the computation of κ and τ , explicit expressions may be used, see Hu et al. (2011). The resulting functions $\kappa : [0, 1] \rightarrow \mathbb{R}$ and

$\tau : [0, 1] \rightarrow \mathbb{R}$ uniquely determine the curve $x = \{x(s), s \in [0, 1]\}$ which can be reconstructed using the Frenet-Serret formulas given in Eqs. (1) – (3).

2.2.2 Discrete Sampling

Exploiting the formulas mentioned above to compute curvature and torsion along a given discrete curve, e.g. representing a fiber, poses additional challenges. Naively computing κ and τ at each sampling point and estimating the required derivatives by means of adjacent sampling points leads to huge errors when reconstructing the original curve from the resulting sequences of curvature and torsion. This can partly be overcome by first interpolating the sampling points using, e.g., splines and then calculating κ and τ on a much finer grid along the spline. However, an exact representation of the spline (or discrete curve) can never be achieved and a good representation requires an infeasible high amount of points at which κ and τ are computed. Of course, using spline representations, κ and τ could be computed explicitly, but a piecewise functional representation of κ and τ would not be suitable for modeling.

For a meaningful definition of κ and τ on discrete curves, adaptations of the Frenet-Serret formulas given in Eqs. (1) – (3) exist (Hu et al., 2011). For a discrete curve given by a sequence of points $r_1, \dots, r_n \in \mathbb{R}^3$, the *discrete Frenet frame* at the vertex r_i is given by

$$t_i = \frac{r_{i+1} - r_i}{|r_{i+1} - r_i|}, \quad (4)$$

$$b_i = \frac{t_{i-1} \times t_i}{|t_{i-1} \times t_i|}, \quad (5)$$

$$n_i = b_i \times t_i, \quad (6)$$

where $i = 1, \dots, n - 1$. Note that b_i and n_i cannot be computed when the unit vectors t_i and t_{i-1} are parallel. In this case, we can simply set $b_i = b_{i-1}$ and compute n_i accordingly. For any $i \in \{1, \dots, n - 1\}$, the curvature $\psi_i \in [0, \pi]$ (also known as “bond angle” in the discrete case)

and the torsion angle $\theta_i \in [-\pi, \pi]$ between r_i and r_{i+1} are then given by

$$\cos \psi_i = t_{i+1} \cdot t_i, \quad \text{and} \quad \cos \theta_i = b_{i+1} \cdot b_i. \quad (7)$$

Furthermore, the unit vector b_i is perpendicular to the ‘‘osculating’’ plane at r_i , i.e., the plane spanned by the vertices r_{i-1}, r_i, r_{i+1} . Thus, the torsion angle θ_i is the angle between the osculating planes at r_i and r_{i+1} .

A discrete version of the Frenet-Serret equations stated in (1) – (3), which is consistent with the above definition of the Frenet frame in Eqs. (4) – (6), is given by

$$\begin{pmatrix} n_{i+1} \\ b_{i+1} \\ t_{i+1} \end{pmatrix} = \mathcal{R}(\theta_i, \psi_i) \begin{pmatrix} n_i \\ b_i \\ t_i \end{pmatrix} \quad (8)$$

for some transfer matrix $\mathcal{R}(\theta_i, \psi_i) \in \mathbb{R}^3 \times \mathbb{R}^3$. For further details, see Hu et al. (2011).

In contrast to naively discretized versions of the continuous Frenet-Serret formulas given in Eqs. (1) – (3), the formulas stated in (4) – (6) and (8), respectively, provide tools for defining curvature ψ_i (bond angle) and torsion θ_i at each (inner) point r_i with $i = 1, \dots, n-1$ of a discrete curve given by the sequence $r_0, \dots, r_n \in \mathbb{R}^3$, which can be used for precisely reconstructing the curve from the sequence of bond and torsion angles ψ_i and θ_i . Note, however, that for uniquely defining a curve by bond and torsion angles, additionally the initial points r_0, r_1, r_2 and the arclengths $|r_{i+1} - r_i|$ between points r_i and r_{i+1} are needed. For simplicity, we choose a constant arclength, i.e., $|r_{i+1} - r_i| = c$, thereby significantly reducing the number of values necessary to describe the curve.

Using the tools stated above, we can essentially (up to a Galilean transformation) describe a curved fiber by a sequence $(\psi_1, \theta_1), \dots, (\psi_{n-1}, \theta_{n-1}) \in [0, \pi] \times [-\pi, \pi]$ of bond and torsion angles. Such sequences will form the basis for our stochastic fiber model, which will be explained in the following section.

Note that the description by a sequence of bond and torsion angles can also be used for planar fibers which can be observed in various nonwovens composed of, e.g., spunbound (Chen et al., 2020) and meltblown (Gahan & Zguris, 2000; Hiremath & Bhat, 2015) fibers. For fully planar fibers, the torsion angle would be 0 at all points and their geometry would be fully given by the sequence of bond angles. However the data at hand comprises fibers for which modeling the torsion angles is essential as they significantly deviate from any given plane.

2.3 Markov Chain Model

Using the representation of curved fibers described in the previous section, we model a fiber as a realization of a sequence of two-dimensional random vectors $(\Psi_1, \Theta_1), (\Psi_2, \Theta_2), \dots : \Omega \rightarrow [0, \pi] \times [-\pi, \pi]$, which are given on some common probability space $(\Omega, \mathcal{F}, \mathbb{P})$.

Assuming no global constraints act on the fibers, we expect the behavior of the fiber at a given point to be conditionally independent of that at points “far away”. More formally, we assume that the random vector $X_j = (\Psi_j, \Theta_j)$ is conditionally independent of $X_i = (\Psi_i, \Theta_i)$ if $j > i + k$ for some order of dependence $k \geq 1$, under the condition that the values of the random vectors $X_{j-1} = (\Psi_{j-1}, \Theta_{j-1}), \dots, X_{j-k} = (\Psi_{j-k}, \Theta_{j-k})$ are given. Furthermore, we assume that the fibers behave statistically in the same way at any sampling point r_1, r_2, \dots , i.e., we assume that the random sequence $\{X_i, i = 1, 2, \dots\}$ is stationary, which means that for each $m \geq 0$ the distribution of the $2(m + 1)$ -dimensional random vector (X_i, \dots, X_{i+m}) does not depend on the choice of $i \in \{1, 2, \dots\}$. Moreover, for the sake of simplicity, we assume that the distribution of (X_1, \dots, X_{1+m}) is absolutely continuous with some probability density $f_{X_1, \dots, X_{1+m}} : \mathbb{R}^{2(m+1)} \rightarrow [0, \infty)$.

Under these assumptions, a (discrete-time) k -th order *Markov chain*, see e.g. Raftery (1985), with the (continuous) two-dimensional state space $[0, \pi] \times [-\pi, \pi]$ seems to be suitable for modeling the random sequence $\{X_i, i = 1, 2, \dots\}$ of bond and torsion angles. Note that higher-order Markov chains extend the concept of an ordinary (first order) Markov chain to allow for memories of any finite length $k \geq 1$.

In order to fit the k -th order Markov chain $\{X_i, i = 1, 2, \dots\}$ to data and to draw samples from the fitted Markov chain model, i.e., to generate synthetic fibers, we determine the multivariate probability density $f_{X_1, \dots, X_{1+k}}$ using the copula approach explained in the next section. Then, we can simulate the random vector (X_1, \dots, X_{1+k}) by drawing a sample (x_1, \dots, x_{1+k}) from the (unconditional) density $f_{X_1, \dots, X_{1+k}}$. In the next step, we simulate the random vector X_{k+2} by drawing a sample x_{k+2} from the (conditional) density $f_{X_{k+2}|X_2=x_2, \dots, X_{1+k}=x_{1+k}} : \mathbb{R}^2 \rightarrow [0, \infty)$, and so on.

2.4 R-Vine Copulas

For modeling fibers by a k -th order Markov chain $\{X_i, i = 1, 2, \dots\}$, the joint distribution of the random vector (X_1, \dots, X_{1+k}) needs to be determined. Using the transformations introduced in Section 2.2, we can generate a large family of sequences x_1, \dots, x_{n-1} from measured data, where $x_i = (\psi_i, \theta_i)$ for $i = 1, \dots, n-1$ and $n-1 > k+1$, which we assume to adhere to the (unknown) distribution of (X_1, \dots, X_{1+k}) . For a parameter-free model of this distribution, we could apply a kernel density estimator (Scott, 2015). This would allow for easy conditional sampling as required by the Markov model. However, later adjustments to the resulting model would be infeasible using this approach. As a benefit of a stochastic fiber model consists in the capability of simulating a wide spectrum of realistic, yet (statistically) different from observed, fibers, a parametric model is desirable. Therefore, we choose to parametrically model the joint probability density $f_{X_1, \dots, X_{1+k}} : \mathbb{R}^{2(k+1)} \rightarrow [0, \infty)$ of (X_1, \dots, X_{1+k}) .

2.4.1 Sklar's Representation Formula

Approaches for parametric modeling of multidimensional vector data include multivariate Gaussian distributions or mixtures thereof (Reynolds, 2009) and so-called copula models. Copulas provide means to model the correlation structure of a multivariate distribution when the marginal distributions are non-Gaussian. For any integer $d \geq 2$, a d -variate *copula* $C : [0, 1]^d \rightarrow [0, 1]$ is the cumulative distribution function of a d -dimensional random vector

(U_1, \dots, U_d) with marginal distributions being equal to the (standard) uniform distribution on $[0, 1]$. Note that a copula essentially describes the interdependence of the components of the corresponding random vector (U_1, \dots, U_d) . Furthermore, copulas lend themselves to modeling of multivariate distributions by *Sklar's representation formula* (Nelsen, 2006), which states that the cumulative distribution function $F_Y : \mathbb{R}^d \rightarrow [0, 1]$ of an arbitrary random vector $Y = (Y_1, \dots, Y_d) : \Omega \rightarrow \mathbb{R}^d$, where $F_Y(y_1, \dots, y_d) = \mathbb{P}(Y_1 \leq y_1, \dots, Y_d \leq y_d)$ for any $y_1, \dots, y_d \in \mathbb{R}$, can be given by the univariate cumulative distribution functions F_{Y_1}, \dots, F_{Y_d} of the components Y_1, \dots, Y_d and a certain d -variate copula C . More precisely, it holds that

$$F_Y(y_1, \dots, y_d) = C(F_{Y_1}(y_1), \dots, F_{Y_d}(y_d)) \quad (9)$$

for any $y_1, \dots, y_d \in \mathbb{R}$. Vice versa, for any d -variate copula C and univariate cumulative distribution functions F_{Y_1}, \dots, F_{Y_d} , the expression given at the right-hand side of Eq. (9) is the cumulative distribution function of a d -dimensional random vector. For differentiable cumulative distributions functions and copulas, Eq. (9) implies that

$$f_Y(y_1, \dots, y_d) = c(F_{Y_1}(y_1), \dots, F_{Y_d}(y_d)) \prod_{i=1}^d f_{Y_i}(y_i) \quad (10)$$

for any $y_1, \dots, y_d \in \mathbb{R}$, where f_Y and f_{Y_i} denote the probability density of the random vector Y and its i -th component Y_i , respectively. Furthermore, the function $c : [0, 1]^d \rightarrow [0, \infty)$ is the probability density corresponding to the copula C .

2.4.2 The Pair-Copula Construction Method

Using Eq. (10), we can model the density of a d -dimensional random vector by modeling its marginal densities in a first step, and a copula density describing the interdependence of its component in a second step. While, in principle, this approach is valid independently of the dimension $d \geq 2$, direct parametric modeling of copulas becomes increasingly hard for high dimensions. However, a way out of this dilemma consists in the utilization of so-called R-

vine copulas (Czado, 2019; Joe, 2014), a flexible parametric model to construct multivariate probability densities by decomposing them into several bivariate conditional (and univariate) densities to fit probability densities to available data. For this, many parametric families of bivariate copulas can be used. In the present paper, we consider the following bivariate copula types when fitting R-vine copulas to data: Gaussian, Student t, Clayton, Gumbel, Frank, Joe, BB1, BB6, BB7, BB8 and their rotations. For more details, see Joe (2014); Nelsen (2006).

The basic idea of this decomposition, illustrated for a three-dimensional random vector $Y = (Y_1, Y_2, Y_3)$, is motivated by the observation that the density $f_Y: \mathbb{R}^3 \rightarrow [0, \infty)$ of Y can be decomposed into a product of the conditional density $f_{Y_1, Y_2|Y_3=y_3}: \mathbb{R}^2 \rightarrow [0, \infty)$ of (Y_1, Y_2) given that $Y_3 = y_3$ and the univariate density $f_{Y_3}: \mathbb{R} \rightarrow [0, \infty)$ of Y_3 , i.e., for each $y = (y_1, y_2, y_3) \in \mathbb{R}^3$ with $f_Y(y) > 0$ it holds that

$$f_Y(y) = f_{Y_1, Y_2|Y_3=y_3}(y_1, y_2)f_{Y_3}(y_3). \quad (11)$$

Inserting Eq. (10) for $d = 2$ into the first factor on the right-hand side of Eq. (11), we get that

$$f_Y(y) = c_{1,2|Y_3=y_3}(F_{Y_1|Y_3=y_3}(y_1), F_{Y_2|Y_3=y_3}(y_2))f_{Y_1|Y_3=y_3}(y_1)f_{Y_2|Y_3=y_3}(y_2)f_{Y_3}(y_3),$$

where $c_{1,2|Y_3=y_3}$ is the density of the copula corresponding to the conditional bivariate density $f_{Y_1, Y_2|Y_3=y_3}$ and $F_{Y_i|Y_3=y_3}$ is the conditional cumulative distribution function of Y_i given that $Y_3 = y_3$ with density $f_{Y_i|Y_3=y_3}$, $i = 1, 2$. Furthermore, using the identity $f_{Y_i|y_3=y_3}(y_i) = f_{Y_i, y_3}(y_i, y_3)/f_{Y_3}(y_3)$ and inserting Eq. (10) for $d = 2$ into the first factor on the right-hand side of this identity, we finally get a pair-copula representation of the three-variate density f_Y , i.e., for each $y = (y_1, y_2, y_3) \in \mathbb{R}^3$ with $f_Y(y) > 0$ it holds that

$$f_Y(y) = c_{1,2|Y_3=y_3}(F_{Y_1|y_3=y_3}(y_1), F_{Y_2|Y_3=y_3}(y_2))c_{1,3}(F_{Y_1}(y_1), F_{Y_3}(y_3))c_{2,3}(F_{Y_2}(y_2), F_{Y_3}(y_3)) \\ \times f_{Y_1}(y_1)f_{Y_2}(y_2)f_{Y_3}(y_3),$$

where $c_{i,3}$ is the copula density corresponding to f_{Y_i, Y_3} , $i = 1, 2$. Note that in general the bivariate copula density $c_{1,2|Y_3=y_3}$ depends on the numerical value of y_3 . However, for computational feasibility, the following simplifying assumption is made, which states that $c_{1,2|Y_3=y_3}$ does not depend of the given value y_3 of Y_3 , but just on the subscript of the component Y_3 appearing in the condition, i.e. $c_{1,2|Y_3=y_3} = c_{1,2|3}$, see Haff et al. (2010).

The pair-copula construction approach described above can be generalized to higher-dimensional random vectors such that similar representation formulas for the density f_Y of a d -dimensional random vector as product of marginal densities and bivariate copula densities can be derived for $d > 3$ as well, see e.g. Czado (2019). In this way, using so-called *regular vines* (shortly: R-vines), a representation can be constructed where the resulting model of f_Y can be fitted to empirical data. For more details, we refer e.g. to two recent case studies (Aigner et al., 2022; Furat et al., 2022), where R-vine copulas have been used to model image data on two completely different (geographical and microscopic) length scales. More precisely, in Aigner et al. (2022) R-vine copulas have been exploited for model-based prediction of uncertain power supply in an electrical distribution network, in order to optimize the discrete curtailment of solar feed-in into the network and to guarantee network stability under fluctuating feed-in, whereas in Furat et al. (2022) R-vine copulas have been used to determine the multivariate probability distribution of descriptor vectors for the size, shape, texture and composition of micron-sized mineral particles.

In the present paper, we use R-vine copulas to parametrically model the multivariate probability density $f_{X_1, \dots, X_{1+k}}$ of the random vector (X_1, \dots, X_{1+k}) appearing in the k -th order Markov chain $\{X_i, i = 1, 2, \dots\}$ introduced in Section 2.3.

2.5 Validation Measures

Model validation is performed by drawing a large number of simulated fibers from the fitted Markov model. Visual comparison of simulated and measured fibers may only indicate a rough resemblance. Thus, in addition to visual inspection, we compute various characteristics for

comparing simulated to measured fibers and thereby quantitatively validating the stochastic fiber model. In particular, we compute and compare the autocorrelation functions of bond and torsion angles, the curl-index of fibers in the three-dimensional Euclidean space \mathbb{R}^3 , and the volume and surface of their convex hulls.

2.5.1 Autocorrelation Function

The *autocorrelation function* $\rho : \{1, 2, \dots\} \times \{1, 2, \dots\} \rightarrow [-1, 1]$ of a (real-valued) stochastic process $\{Y_i, i = 1, 2, \dots\}$ describes the correlation between the states Y_{i_1} and Y_{i_2} of the process at different instants $i_1, i_2 \geq 1$. While in the literature there are various slightly different definitions of this notion (Park, 2018), we choose the definition based on the Pearson correlation coefficient, i.e., for any integers $i_1, i_2 \geq 1$ it holds that

$$\rho(i_1, i_2) = \frac{\mathbb{E}((Y_{i_1} - \mathbb{E}(Y_{i_1}))(Y_{i_2} - \mathbb{E}(Y_{i_2})))}{\sqrt{\text{Var}(Y_{i_1})\text{Var}(Y_{i_2})}}.$$

Note that for a stationary process $\{Y_i, i = 1, 2, \dots\}$, the value of $\rho(i_1, i_2)$ depends only on the length of $\tau = |i_1 - i_2|$ of the interval (i_1, i_2) and can be written as

$$\rho(\tau) = \frac{\mathbb{E}((Y_{i+\tau} - \mu)(Y_i - \mu))}{\sigma^2},$$

where $\mu = \mathbb{E}(Y_1)$ and $\sigma^2 = \text{Var}(Y_1)$. Note that $\rho(0) = 1$ always holds by definition.

For a given $\tau \geq 1$, we can estimate $\rho(\tau)$ from a collection of n arbitrarily truncated independent realizations $(y_{1,1}, \dots, y_{1,m_1}), \dots, (y_{n,1}, \dots, y_{n,m_n})$ of the stochastic process $\{Y_i, i = 1, 2, \dots\}$ by compiling a set S of all pairs of values $(y_{i,j}, y_{i,j+\tau})$ and computing the Pearson correlation coefficient on this set.

2.5.2 Curl-Index of Fibers

The *curl-index* $c \in [1, \infty]$ as introduced by Kallmes & Corté (1960) for fibers in \mathbb{R}^3 , represented by a sequence of points $r_0, \dots, r_n \in \mathbb{R}^3$, is given by

$$c = \frac{\sum_{i=0}^{n-1} |r_{i+1} - r_i|}{|r_n - r_0|}.$$

Note that this descriptor is related to the so-called geodesic tortuosity (Neumann et al., 2019) which is often applied to characterize the “windedness” of transportation paths in porous media. Obviously, the curl-index may be affected by the overall length of the fiber. Thus, when comparing two sets of fibers, we need to make sure that the distribution of fiber length is similar for both sets. However, since we assume stationarity of the underlying stochastic fiber model, see Section 2.3, we can randomly cut segments of a given length from all fibers to achieve comparability.

2.5.3 Descriptors of Convex Hull

The *convex hull* of a fiber, represented by a sequence of points $r_0, \dots, r_n \in \mathbb{R}^3$, is the convex set minimizing its volume while containing the entire fiber, i.e., containing all points $r_0, \dots, r_n \in \mathbb{R}^3$. For a discretized fiber, this is always a convex polytope and algorithms for efficient computation of the convex hull, e.g., the QuickHull algorithm (Barber et al., 1996), exist. We can determine various descriptors of the convex hull, including its volume and surface area, which we will use for comparing two sets of fibers. Again, these measures are affected by the overall length of fibers and we need to adjust in a similar way as mentioned above in Section 2.5.2.

3 Results & Discussion

From the tomographic image data described in Section 2.1, we use 1117 fibers for model fitting and validation. The lengths of these fibers varied significantly with a minimum length

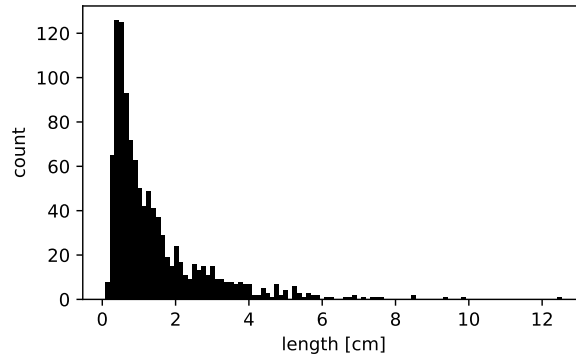


Fig. 2. Histogram of fiber lengths.

of 3.03 mm, a maximum length of 126.5 mm and a mean length of 14.4 mm. Fig. 2 shows a histogram of fiber lengths.

Based on this data, we calibrate the parameters of the stochastic fiber model which is built by means of the three modeling components (Frenet representation, Markov chain, vine copula) described in Sections 2.2 – 2.4. In particular, by drawing samples from a k -th order Markov chain, we generate polygonal fiber tracks via their Frenet representation, i.e., the sequence of bond and torsion angles along the fibers. A crucial step of the model fitting procedure is the selection of an appropriate transition kernel of the Markov chain, where an R-vine copula is used to capture the correlation structure of the underlying data. From the simulated sequences of bond and torsion angles, we then compute the coordinates of the vertices of polygonal tracks representing the fibers. Finally, we evaluate the suitability of the Frenet representation and the performance of the stochastic fiber model.

3.1 Frenet Representation

Transforming the data described in Section 2.1 by means of the methods from Section 2.2 yields two sequences $\psi_1, \dots, \psi_{n-1}$ and $\theta_1, \dots, \theta_{n-1}$ for each fiber, representing the bond angle $\psi_i \in [0, \pi]$ and the torsion angle $\theta_i \in [-\pi, \pi]$ at each (discrete) sampling point r_i along the fiber. Vice versa, vertices of the fiber can be computed from the initial Frenet frame and the sequence of bond and torsion angles. Recall that the results of these computations depend on the distances $d_i = |r_{i+1} - r_i|$ between adjacent sampling points which we assume to be

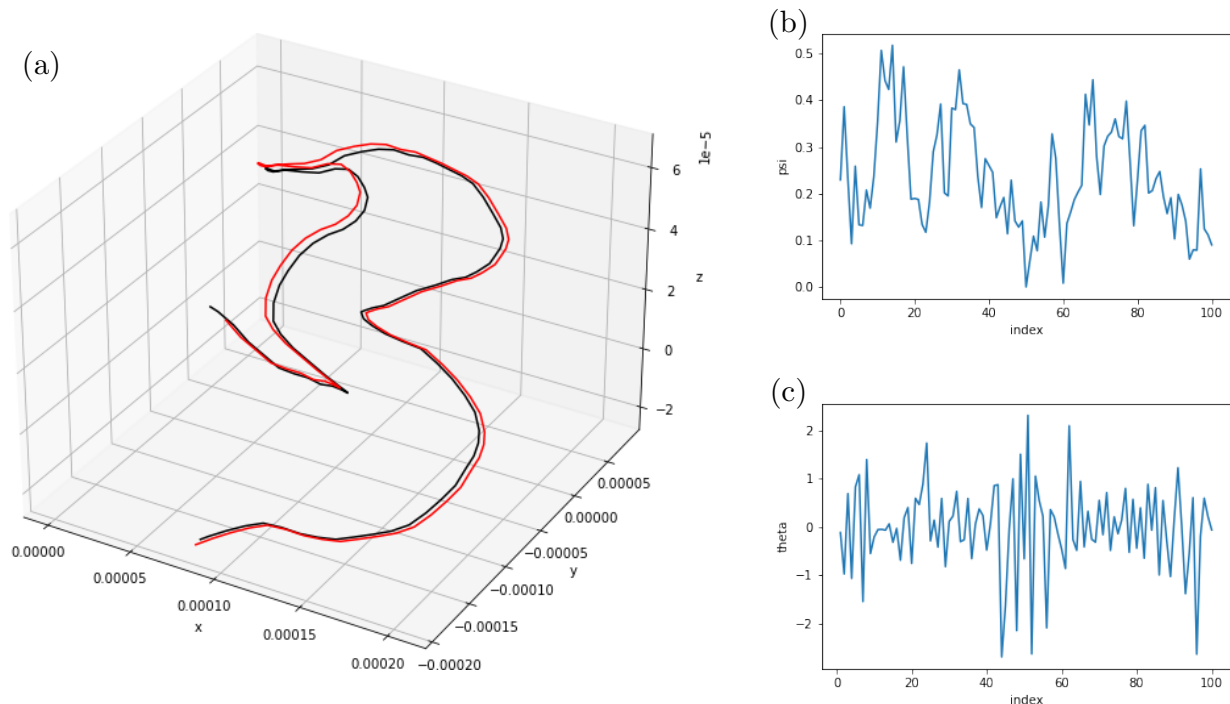


Fig. 3. (a) Example of a fiber given by a polygonal chain which has been extracted from experimental data (black). (b) Bond angle ψ_i along the chain. (c) Torsion angle θ_i along the chain. The polygonal chain reconstructed from curvature and torsion nicely coincides with the original polygonal chain as shown in red in (a).

constant. Numerical errors may lead to deviations from this assumption and may further negatively affect the computation of Frenet frames as well as bond and torsion angles. We assess these errors by computing the sequence $(\psi_1, \theta_1), \dots, (\psi_{n-1}, \theta_{n-1})$ of bond and torsion angles (ψ_i, θ_i) and the initial Frenet frame (t_0, n_0, b_0) of a fiber represented by the sampling points r_0, \dots, r_n and re-transform this representation into Euclidean coordinates denoted by $\hat{r}_0, \dots, \hat{r}_n$. Fig. 3 shows an example of a fiber extracted from tomographic image data (black) along with the computed bond and torsion angles and the re-transformed fiber (red).

The visual impression of good correspondence between original and reconstructed fibers is confirmed when computing the re-transformations for all fibers extracted from tomographic image data. In Fig. 4, the distances $|\hat{r}_i - r_i|$ are visualized for each pair of sampling points r_i, \hat{r}_i along the fibers. The solid line represents the mean error averaged over all fibers, and

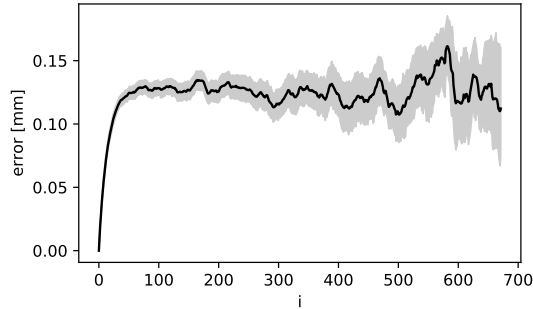


Fig. 4. Deviation between pairs of sampling points for original and reconstructed fibers.

the errors for 99% of all fibers fall within the light gray band. For a fiber with length equal to the mean length of 14.4 mm, the error would never exceed 1.3% of its length.

3.2 Model Fitting

The starting point when constructing the stochastic fiber model described in Sections 2.3 and 2.4 consists of suitably selecting parametric models for the univariate probability densities of bond and torsion angles. For this, we first consider two samples containing all bond angles and all torsion angles, respectively. It turns out that the family of inverse Gaussian distributions leads to a good fit for the bond angles, whereas the family of normal inverse Gaussian distributions is chosen for the torsion angles. Note that we select these two types of parametric distributions from an extensive range of over 100 families of distributions given by the python package SciPy (Virtanen et al., 2020), by assessing the goodness of fit.

Recall that the probability density function $f_\mu : [0, \infty) \rightarrow [0, \infty)$ of the inverse Gaussian distribution with parameter $\mu > 0$ is given by

$$f_\mu(x) = \frac{1}{\sqrt{2\pi x^3}} \exp\left(-\frac{(x - \mu)^2}{2x\mu^2}\right)$$

for each $x \geq 0$. To allow for more flexibility, we additionally introduce a location parameter $l \in \mathbb{R}$ as well as a scale parameter $s > 0$ and define the probability density function $f_{\mu,s,l} :$

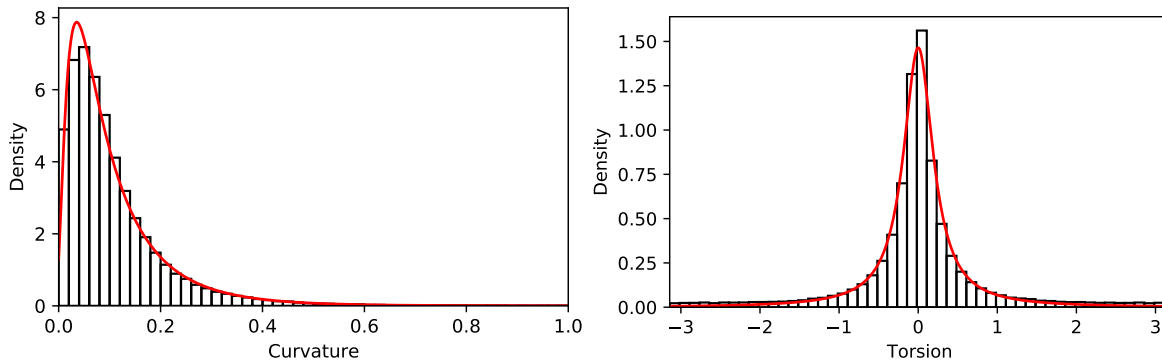


Fig. 5. Histograms of measured data (black) and fitted parametric densities (red) for bond angles (left) and torsion angles (right).

$[s, \infty) \rightarrow [0, \infty)$ of the (generalized) inverse Gaussian distribution by

$$f_{\mu,s,l}(x) = \frac{1}{s} f_{\mu} \left(\frac{x-l}{s} \right)$$

for each $x \geq l$. Furthermore, the probability density function $f_{a,b} : \mathbb{R} \rightarrow [0, \infty)$ of the normal inverse Gaussian distribution with parameters $a > 0$ and $|b| \leq a$ is given by

$$f_{a,b}(x) = \frac{a K_1(a\sqrt{1+x^2})}{\pi\sqrt{1+x^2}} \exp \left(\sqrt{a^2 - b^2} + bx \right)$$

for each $x \in \mathbb{R}$. Here, $K_1 : [0, \infty) \rightarrow [0, \infty)$ is the modified Bessel function of second kind (Abramowitz et al., 1988). Again, we generalize the density function $f_{a,b}$ by introducing location and scale parameters s and l , modifying the function $f_{a,b}$ in the same way as described above in the case of the inverse Gaussian distribution. Fitting these probability density functions to measured data described in Section 2.1 by maximum likelihood estimation, the following values have been obtained for the 7 model parameters: $\mu = 0.6446$, $l = -0.0175$ and $s = 0.1932$ for the inverse Gaussian distribution describing the bond angles, and $a = 0.0557$, $b = 0.0002$, $l = 0.0007$ and $s = 0.2286$ for the normal inverse Gaussian distribution describing the torsion angles. Fig. 5 shows histograms of measured data as well as the parametric probability densities fitted to this data.

In a second step, the Markov chain model described in Section 2.3 has been fitted, which requires to choose the integer-valued parameter k specifying the length of memory. This parameter then affects the subsequently fitted copula, in particular the dimension of the multivariate distribution which is needed for modeling the transition kernel of the k -th order Markov chain. Initially, we chose $k = 1, \dots, 5$ as candidates. Thus, for each $k \in \{1, \dots, 5\}$, an R-vine copula has been fitted to capture the correlation structure present in measured data, applying the pair-copula construction method briefly explained in Section 2.4.2 and using the univariate parametric (marginal) densities described above. Then, by means of the fitted k -th order Markov chain, 250 fibers are simulated for each value of $k = 1, \dots, 5$. It turns out that already $k = 2$ yields satisfactory results while keeping the computational complexity and the amount of required data low. For visual assessment, Fig. 6 shows examples of fibers extracted from tomographic image data alongside with simulated fibers and their respective functions of bond and torsion angles for $k = 2$. Visually, there are no obvious flaws in the simulated fibers. On the contrary, the overall shape seems to match the measured data well.

3.3 Model Validation

The validation measures described in Section 2.5 are computed for each value of $k \in \{1, \dots, 5\}$. Moreover, 250 simplified “reference fibers” are simulated, where torsion and bond angles are drawn independently from the fitted univariate densities, see Fig. 5, i.e., no correlations along the fibers are taken into account. We use these simplified fibers for comparison, to show the suitability of the vine copula approach described in Section 2.4 for the stochastic modeling of measured fibers.

Fig. 7 shows autocorrelation functions computed for measured and simulated sequences of bond and torsion angles. Even though, in the following, we only discuss the k -th order Markov chain model for $k = 1, \dots, 5$, we found that also for $k > 5$ the autocorrelation functions of simulated fibers match those of measured fibers quite well. Note, however, that for the simplified reference fibers, the values $\rho(\tau)$ of both autocorrelation functions $\rho : \{0, 1, \dots\} \rightarrow$

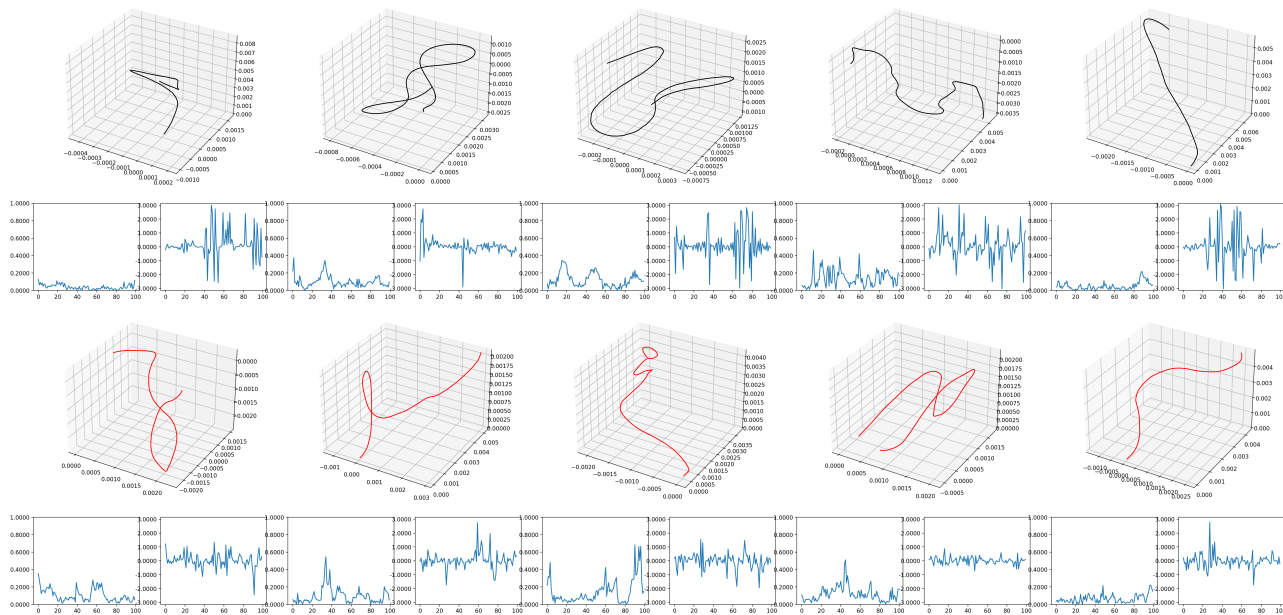


Fig. 6. Top: Five fibers selected at random from measured data and truncated at 100 steps. Bottom: Five simulated fibers. Below each fiber, the corresponding bond angles (left) and torsion angles (right) along the fiber are shown.

$[-1, 1]$ for bond and torsion angles would be equal to 1 for $\tau = 0$ by definition, but 0 for any $\tau > 0$ which is in clear contrast to the autocorrelation functions obtained from measured data, at least for the sequence of bond angles, see the left-hand side of Fig. 7.

To evaluate the goodness of model fit by means of the curl-index and the convex-hull descriptors stated in Section 2.5, we cut random segments with lengths of 0.3, 0.6, 1 and 1.5 mm from all fibers and compute kernel density estimates for the probability densities of the resulting samples of validation measures, see Figs. 8, 9 and 10. For comparison, the estimated densities obtained for the simplified reference fibers (without taking account of the correlations along the fibers) are shown in gray. It is clearly visible that the incorporation of correlation effects into the stochastic fiber model, via the vine copula approach described in Section 2.4, has a huge beneficial impact on the goodness of fit. In particular, for segments with lengths greater than 0.3 mm, we see large deviations of the descriptors considered in Figs. 8, 9 and 10 for the simplified reference fibers from those of measured fibers, while the

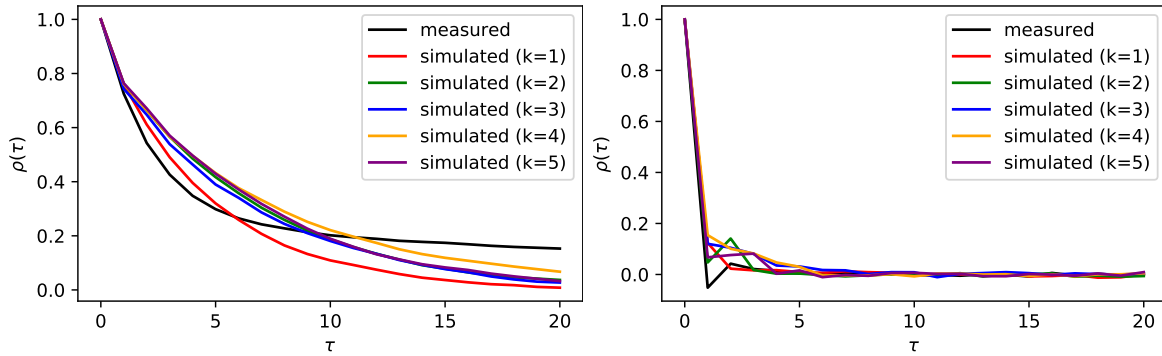


Fig. 7. Estimated autocorrelation functions for bond (left) and torsion angles (right). Black curves show the autocorrelation functions obtained from measured data, whereas colored curves show those obtained for the k -th order Markov model with $k = 1, \dots, 5$.

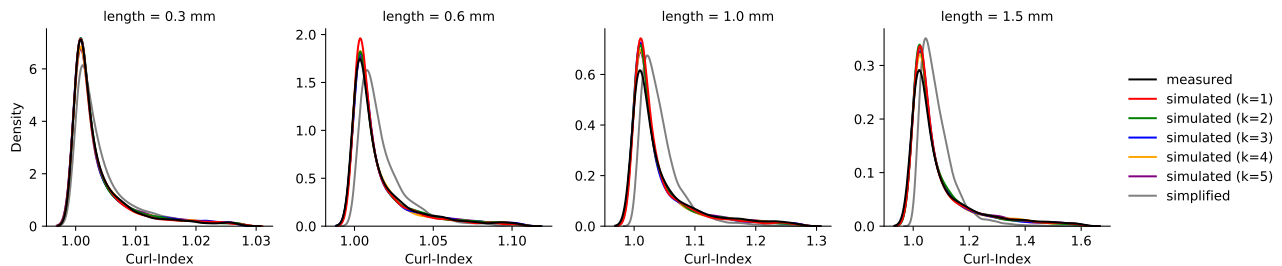


Fig. 8. Density functions of the curl-index of randomly selected fiber segments for four different lengths. Black curves show the density functions obtained from measured data, colored curves those obtained from the k -th order Markov models with $k = 1, \dots, 5$. The gray curves show the density function obtained from the reference fibers.

fibers generated by means of the copula approach show a good fit to measured data.

Visual inspection of Figs. 8, 9 and 10 gives the impression that the probability densities shown in these figures are largely independent of the specific choice of the model parameter $k \in \{1, \dots, 5\}$. To evaluate this in more detail, we consider the Kolmogorov-Smirnov statistic $D : \mathbb{R}^{2n} \rightarrow [0, 1]$, which is given by $D(z, z') = \sup_{y \in \mathbb{R}} |F(y) - F'(y)|$ for arbitrary samples $z = (z_1, \dots, z_n) \in \mathbb{R}^n$ and $z' = (z'_1, \dots, z'_n) \in \mathbb{R}^n$, where F and F' denote the empirical cumulative distribution functions corresponding to z and z' , respectively. As an example, Tab. 1 shows the numerical results which have been obtained for $D(z, z')$ if z and z' are samples of convex-hull surface areas of measured and simulated fiber fragments.

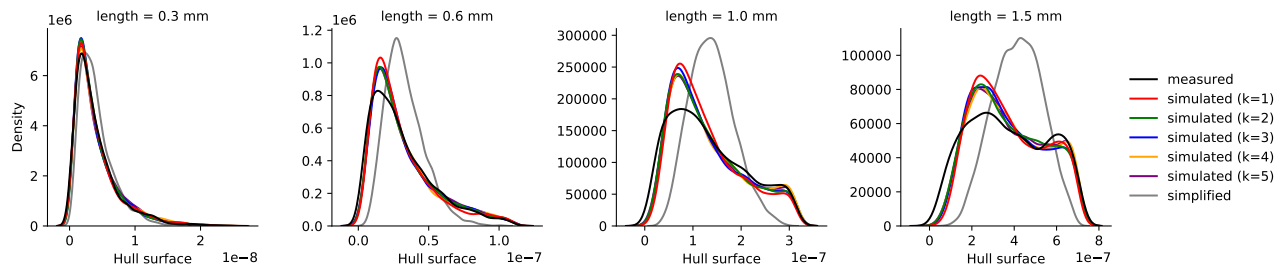


Fig. 9. Density functions of the convex-hull surface area of randomly selected fiber segments for four different lengths. Black curves show the density functions obtained from measured data, colored curves those obtained from the k -th order Markov models with $k = 1, \dots, 5$. The gray curves show the density function obtained from the reference fibers.

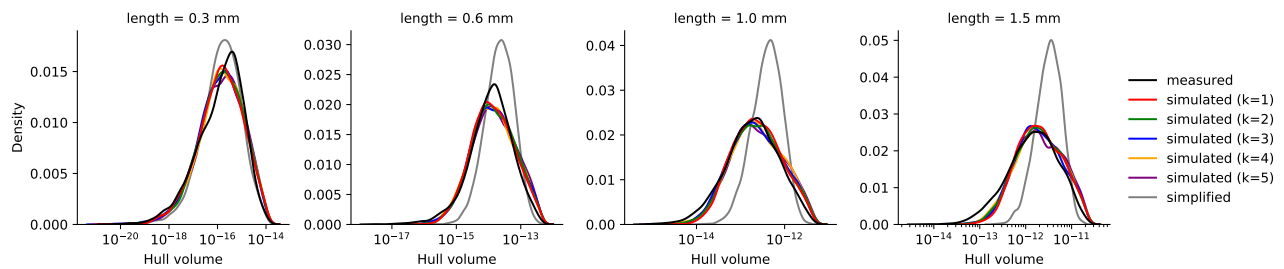


Fig. 10. Density functions of the convex-hull volume of randomly selected fiber segments for four different lengths. Black curves show the density functions obtained from measured data, colored curves those obtained from the k -th order Markov models with $k = 1, \dots, 5$. The gray curves show the density function obtained from the reference fibers.

segment length	0.3 mm	0.6 mm	1.0 mm	1.5 mm
k				
1	0.0248	0.0490	0.0608	0.0600
2	0.0156	0.0470	0.0494	0.0508
3	0.0326	0.0434	0.0504	0.0570
4	0.0194	0.0474	0.0456	0.0554
5	0.0138	0.0448	0.0494	0.0472
reference fibers	0.1212	0.2368	0.2480	0.2522

Table 1. Kolmogorov-Smirnov statistic for samples of the convex-hull surface area of measured and simulated fiber segments, for four different segment lengths and $k = 1, \dots, 5$. For comparison, values of the Kolmogorov-Smirnov statistic are given, which have been obtained for the simplified reference fibers.

While the values of the Kolmogorov-Smirnov statistic given in Tab. 1 do not differ much from each other for different values of $k \in \{2, \dots, 5\}$, they seem to be higher for $k = 1$, especially when considering longer fiber segments. Similar observations have been made with respect to the values of the Kolmogorov-Smirnov statistic regarding the curl-index and the convex-hull volume. These findings are in line with the visual impression of the autocorrelation functions for sequences of bond angles which do not significantly differ from each other for $k \in \{2, \dots, 5\}$, but do change when passing from $k = 1$ to $k \geq 2$, see the left-hand side of Fig. 7.

We thus conclude that the k -th order Markov chain model proposed in this paper performs similarly well for each k between 2 and 5, where the overall behavior of measured fibers is nicely captured already for $k = 2$. This is true for the Frenet representation as well as in the Euclidean domain.

4 Conclusions

Modeling single fibers of, e.g., nonwoven materials constitutes a crucial step in the development of stochastic 3D models for fiber systems. These models, when used for digital materials design, require flexibility such that they cover a wide spectrum of virtual, but realistic scenarios. The method proposed in the present paper for describing single fibers as higher-order Markov chains of bond and torsion angles by using discrete Frenet-Serret formulas, shows the desired flexibility via the appropriate choice of the suitable parametric families of univariate densities of bond and torsion angles as well as the adjustment of the transition kernel of the corresponding Markov chain. Since also the transition kernel is parametrically modelled using so-called vine copulas, model fitting to tomographic image data and model variation for subsequent virtual materials testing can be easily achieved. As pointed out in this paper, a 6-variate R-vine copula is capable of capturing the essential structural properties of real fibers sufficiently well. In particular, we fitted our model to experimentally measured data of fibers from a real nonwoven material and performed model validation by comparing descriptors of simulated fibers to those of measured fibers, where we showed that the distributions of bond and torsion angles and their correlations along the fibers nicely match for simulated and measured data. Furthermore, geometrical properties emerging from the representation of fibers in 3D space show a good correspondence between simulated and measured fibers. We conclude that the stochastic single-fiber model proposed in this paper is indeed capable of capturing essential properties of curved fibers of nonwovens.

It turned out that our model performs sufficiently well for a second order Markov chain. Hence, the resulting low number of parameters facilitates its usage in further work. This may include the development of a stochastic 3D model for the entire fiber system of various kinds of nonwovens, accounting for mutual interaction between fibers. Since in our single-fiber model, the fibers are drawn step-by-step from conditional probability distributions, introducing further restraints and requirements should be a relatively easy task. Furthermore, since the

univariate distributions of bond and torsion angles as well as the R-vine copulas accounting for correlations along the fibers can be selected from an extensive range of parametric models, adaptations to various types of fibers can be performed.

While we showed the model using a specific dataset, its inherent flexibility lends itself to explore various other types of fibers. In particular, planar or helical fibers form a special case of the presented approach where the torsion angles are given by a constant value.

References

- Abishek, S., King, A., Mead-Hunter, R., Golkarfarad, V., Heikamp, W. & Mullins, B.** (2017). Generation and validation of virtual nonwoven, foam and knitted filter (separator/coalescer) geometries for CFD simulations, *Separation and Purification Technology* **188**, 493–507.
- Abramowitz, M., Stegun, I.A. & Romer, R.H.** (1988). *Handbook of Mathematical Functions with Formulas, Graphs, and Mathematical Tables*, American Association of Physics Teachers.
- Aigner, K.M., Schaumann, P., von Loeper, F., Martin, A., Schmidt, V. & Liers, F.** (2022). Robust DC optimal power flow with modeling of solar power supply uncertainty via R-vine copulas, *Optimization and Engineering under revision*.
- Ali, M.A., Umer, R. & Khan, K.A.** (2020). A virtual permeability measurement framework for fiber reinforcements using micro CT generated digital twins, *International Journal of Lightweight Materials and Manufacture* **3**, 204–216.
- Altendorf, H. & Jeulin, D.** (2011). Random-walk-based stochastic modeling of three-dimensional fiber systems, *Physical Review E* **83**, 041804.
- Azimian, M., Kühnle, C. & Wiegmann, A.** (2018). Design and optimization of fibrous filter media using lifetime multipass simulations, *Chemical Engineering & Technology* **41**, 928–935.
- Barber, C.B., Dobkin, D.P. & Huhdanpaa, H.** (1996). The quickhull algorithm for convex hulls, *ACM Transactions on Mathematical Software (TOMS)* **22**, 469–483.

- Bartels, R.H., Beatty, J.C. & Barsky, B.A.** (1995). *An Introduction to Splines for Use in Computer Graphics and Geometric Modeling*, Morgan Kaufmann.
- Chen, K., Ghosal, A., Yarin, A.L. & Pourdeyhimi, B.** (2020). Modeling of spunbond formation process of polymer nonwovens, *Polymer* **187**, 121902.
- Czado, C.** (2019). *Analyzing Dependent Data with Vine Copulas*, Springer.
- Furat, O., Kirstein, T., Leißner, T., Bachmann, K., Gutzmer, J., Peuker, U.A. & Schmidt, V.** (2022). Prediction of mineralogical particle composition using CT data and R-vine copulas, *Minerals Engineering* **submitted**.
- Gahan, R. & Zguris, G.C.** (2000). A review of the melt blown process, *Fifteenth Annual Battery Conference on Applications and Advances (Cat. No.00TH8490)*, 145–149.
- Gaiselmann, G., Froning, D., Tötze, C., Quick, C., Manke, I., Lehnert, W. & Schmidt, V.** (2013). Stochastic 3D modeling of non-woven materials with wet-proofing agent, *International Journal of Hydrogen Energy* **38**, 8448–8460.
- Geerling, C., Azimian, M., Wiegmann, A., Briesen, H. & Kuhn, M.** (2020). Designing optimally-graded depth filter media using a novel multiscale method, *AIChE Journal* **66**, e16808.
- Grießer, A., Westerteiger, R., Wagner, C. & Wiegmann, A.** (2019). FiberFind: Machine learning-based segmentation and identification of individual fibers in μ CT images of fibrous media, *International Conference on Tomography of Materials & Structures 2019, Cairns, Australia*.
- Grießer, A., Westersteiger, R. & Boever, W.D.** (2022a). Fibers extracted from nonwoven using FiberFind, <https://doi.org/10.30423/data.math2market-2022-02.sample-c.fiberfind>.
- Grießer, A., Westersteiger, R., Glatt, E., Hagen, H. & Wiegmann, A.** (2022b). Identification and analysis of fibers in ultra-large X-ray scans of nonwoven textiles using deep learning, *Journal of the Textile Institute* **under revision**.
- Haff, I.H., Aas, K. & Frigessi, A.** (2010). On the simplified pair-copula construction—simply useful or too simplistic, *Journal of Multivariate Analysis* **101**, 1296–1310.

- Hiremath, N. & Bhat, G.** (2015). Melt blown polymeric nanofibers for medical applications-an overview, *Nanosci Technol* **2**, 1–9.
- Hu, S., Lundgren, M. & Niemi, A.J.** (2011). Discrete Frenet frame, inflection point solitons, and curve visualization with applications to folded proteins, *Physical Review E* **83**, 061908.
- Huang, X., Zhou, Q., Liu, J., Zhao, Y., Zhou, W. & Deng, D.** (2017). 3D stochastic modeling, simulation and analysis of effective thermal conductivity in fibrous media, *Powder Technology* **320**, 397–404.
- Joe, H.** (2014). *Dependence Modeling with Copulas*, Chapman and Hall/CRC.
- Kallel, H. & Joulain, K.** (2022). Design and thermal conductivity of 3D artificial cross-linked random fiber networks, *Materials & Design* **220**, 110800.
- Kallmes, O.J. & Corté, H.** (1960). The structure of paper, I. The statistical geometry of an ideal two dimensional fiber network, *Tappi J* **43**, 737–752.
- Kroutilova, J., Maas, M., Mecl, Z., Wagner, T., Klaska, F. & Kasparkova, P.** (2020). Bulky nonwoven fabric with enhanced compressibility and recovery, patent WO2020/103964.
- Kühnel, W.** (2015). *Differential Geometry: Curves – Surfaces – Manifolds*, American Mathematical Society, 3rd ed.
- Mao, N., Russell, S.J. & Pourdeyhimi, B.** (2007). Characterisation, testing and modelling of nonwoven fabrics, S.J. Russell (ed.), *Handbook of Nonwovens*, 401–514, Elsevier.
- Moghadam, A., Yousefi, S.H., Tafreshi, H.V. & Pourdeyhimi, B.** (2019). Characterizing nonwoven materials via realistic microstructural modeling, *Separation and Purification Technology* **211**, 602–609.
- Nelsen, R.B.** (2006). *An Introduction to Copulas*, Springer.
- Neumann, M., Hirsch, C., Staněk, J., Beneš, V. & Schmidt, V.** (2019). Estimation of geodesic tortuosity and constrictivity in stationary random closed sets, *Scandinavian Journal of Statistics* **46**, 848–884.

- Park, K.I.** (2018). *Fundamentals of Probability and Stochastic Processes with Applications to Communications*, Springer.
- Raftery, A.E.** (1985). A model for high-order Markov chains, *Journal of the Royal Statistical Society: Series B (Methodological)* **47**, 528–539.
- Reynolds, D.A.** (2009). Gaussian mixture models., *Encyclopedia of Biometrics* **741**, 659–663.
- Schladitz, K., Peters, S., Reinel-Bitzer, D., Wiegmann, A. & Ohser, J.** (2006). Design of acoustic trim based on geometric modeling and flow simulation for non-woven, *Computational Materials Science* **38**, 56–66.
- Schneider, M.** (2017). The sequential addition and migration method to generate representative volume elements for the homogenization of short fiber reinforced plastics, *Computational Mechanics* **59**, 247–263.
- Schulz, V.P., Becker, J., Wiegmann, A., Mukherjee, P.P. & Wang, C.Y.** (2007). Modeling of two-phase behavior in the gas diffusion medium of PEFCs via full morphology approach, *Journal of the Electrochemical Society* **154**, B419.
- Scott, D.W.** (2015). *Multivariate Density Estimation: Theory, Practice, and Visualization*, J. Wiley & Sons.
- Soltani, P., Azimian, M., Wiegmann, A. & Zarrebini, M.** (2018). Experimental and computational analysis of sound absorption behavior in needled nonwovens, *Journal of Sound and Vibration* **426**, 1–18.
- Soltani, P., Zarrebini, M., Laghaei, R. & Hassanpour, A.** (2017). Prediction of permeability of realistic and virtual layered nonwovens using combined application of X-ray μ CT and computer simulation, *Chemical Engineering Research and Design* **124**, 299–312.
- Townsend, P., Larsson, E., Karlson, T., Hall, S.A., Lundman, M., Bergström, P., Hansson, C., Lorén, N., Gebäck, T., Särkkä, A. & Röding, M.** (2021). Stochastic modelling of 3D fiber structures imaged with X-ray microtomography, *Computational Materials Science* **194**, 110433.

- Venkateshan, D., Tahir, M., Vahedi Tafreshi, H. & Pourdeyhimi, B. (2016). Modeling effects of fiber rigidity on thickness and porosity of virtual electrospun mats, *Materials & Design* **96**, 27–35.
- Virtanen, P., Gommers, R., Oliphant, T.E., Haberland, M., Reddy, T., Cournapeau, D., Burovski, E., Peterson, P., Weckesser, W., Bright, J., van der Walt, S.J., Brett, M., Wilson, J., Millman, K.J., Mayorov, N., Nelson, A.R.J., Jones, E., Kern, R., Larson, E., Carey, C.J., Polat, İ., Feng, Y., Moore, E.W., VanderPlas, J., Laxalde, D., Perktold, J., Cimrman, R., Henriksen, I., Quintero, E.A., Harris, C.R., Archibald, A.M., Ribeiro, A.H., Pedregosa, F., van Mulbregt, P. & SciPy 1.0 Contributors (2020). SciPy 1.0: Fundamental algorithms for scientific computing in python, *Nature Methods* **17**, 261–272.
- Wiegmann, A. (2008). Effective properties of nonwoven textiles from microstructure simulations, L.L. Bonilla, M. Moscoso, G. Platero & J.M. Vega (eds.), *Progress in Industrial Mathematics at ECMI 2006*, 708–712, Springer.
- Wiegmann, A., Rief, S. & Latz, A. (2007). Computer models of nonwoven geometry and filtration simulation, *Filtration News* **26**, 65–69.
- Zamel, N., Li, X., Shen, J., Becker, J. & Wiegmann, A. (2010). Estimating effective thermal conductivity in carbon paper diffusion media, *Chemical Engineering Science* **65**, 3994–4006.